

*Short Communication*

## **Laser cladding in-situ nano-submicron TiC reinforced ultrafine-grained Fe-based composite layers on 42CrMo steel**

Hui Xu, Yunpeng Lu, Hui Zhang\*, Guangchun Xiao, Wei Zhao

College of mechanical and automotive engineering, Qilu University of Technology (Shandong Academy of Sciences), Jinan, China

\*E-mail: [zhanghui198787@163.com](mailto:zhanghui198787@163.com)

*Received:* 1 July 2019 / *Accepted:* 10 August 2019 / *Published:* 30 August 2019

---

In-situ nano-submicron TiC reinforced ultrafine-grained Fe-based cladding layers were prepared by laser cladding gradient particle sizes of ferrotitanium, graphite, and iron powder on the surface of 42CrMo steel. Microstructures and corrosion resistance were analyzed using X-ray diffraction, scanning electron microscope, and an electrochemical workstation. Results showed that the average particle size of the in-situ TiC was 0.25  $\mu\text{m}$ , and ranged from 0.04  $\mu\text{m}$  to 1.10  $\mu\text{m}$ , with 11.0 % being on the nano scale. The microstructure of the cladding layer was lath martensite, and the average grain size of the cladding layer matrix was 4.08  $\mu\text{m}$ , reaching the ultrafine-grained scale. The average hardness of the cladding layer was approximately 720 HV0.2, which was 425 HV0.2 higher than that of the 42CrMo steel. The corrosion current density of the cladding layer was more than two times lower than that of the 42CrMo steel.

---

**Keywords:** laser cladding; ultrafine-grained; nano-submicron; TiC

### **1. INTRODUCTION**

As a surface strengthening and repairing technology, laser cladding has the advantages of a low dilution ratio, small stress deformation, and metallurgical bonding with the substrate. Laser cladding shows great developmental potential for improving the surface hardness, and the corrosion, and wear resistance of materials [1-3]. Although Co-based and Ni-based cladding layers have good properties, their raw materials are rare and expensive. Fe-based cladding materials have obvious price advantages and are similar to the composition of the substrate, thus, they have broad application prospects.

As an ideal ceramic reinforcing phase, TiC has high hardness, high wear resistance, and stable thermodynamic properties. It had been widely used in metal matrix composite laser cladding layers, such as TiC/Al [4-6], TiC/Ni [7], TiC/Fe [8], TiC/Ti [9], TiC/TiAl [10], and TiC/AlCoCrFeNi high-entropy alloy [11]. It was also reported in other surface modification methods, for instance, TiC plasma-sprayed

coatings [12], TiC/steel gas tungsten arc cladding layers [13], and TiC/Fe<sub>3</sub>Al high-velocity oxy-fuel coatings [14]. Zhang et al. [15] showed that the TiC/Fe cladding layers showed superior erosion resistance to that of the low carbon steel substrate. Xu et al. [16] prepared a TiC reinforced Inconel 625 composite layer on the surface of austenitic stainless steel, which exhibited good corrosion resistance.

In our previous studies [17-19], the microstructure and properties of a TiC-VC reinforced Fe-based cladding layer were studied by optimizing the initial alloy powders particle size. The Ti-V carbides were refined by decreasing the ferrotitanium-ferrovanadium, graphite, and iron powder particle sizes [20]. The laser cladding processing parameters have an important effect on the morphology of in-situ formed TiC [21]. Therefore, the objective of this study was to prepare in-situ nano-submicron TiC reinforced ultrafine-grained Fe-based laser cladding layers using the gradient particle size of initial alloy powders by adjusting the heat input per unit volume.

## 2. MATERIALS AND METHODS

The substrate material used was 42CrMo steel with dimensions of 80 mm × 40 mm × 12 mm. The surface of the samples was ground with abrasive paper and degreased using anhydrous ethanol before cladding. The particle sizes of the Fe-based alloy powder with a composition of 53.33 wt.% FeTi30, 40.27 wt.% reduced iron powder, and 6.4 wt.% graphite (purity 99.5%) powder are listed in Table 1, and the morphologies of the initial alloy powders are shown in Figure 1. The alloy powders were mixed two hours using a V-mixer (24 revolutions per minute), and then blended with sodium silicate binder onto the specimen surface. The thickness of the preset powder layer was approximately 0.4 mm (preset powder layer accuracy achieved by machining a groove with a thickness of 0.4 mm on the surface of the substrate). Laser cladding was performed using a LASERLINE semiconductor laser and the processing parameters of cladding are listed in Table 2.

**Table 1.** Particle size of the initial alloy powders

	Reduced iron powder	FeTi30 powder	Graphite powder
Particle size	75 μm -150 μm	23 μm -38 μm	10 μm -13 μm

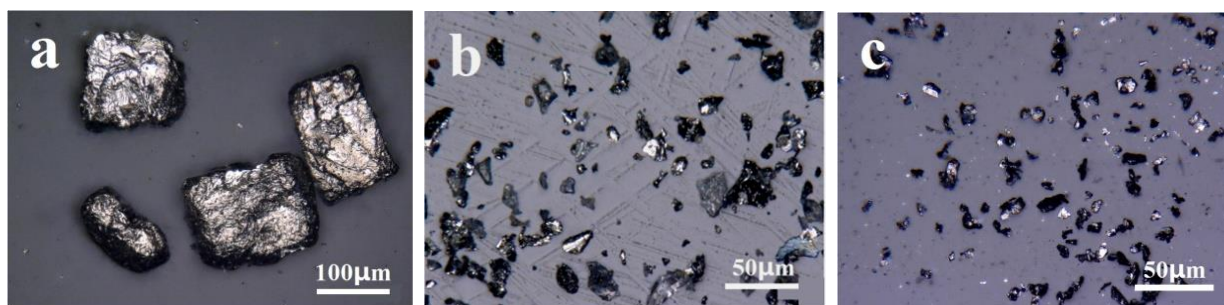


**Figure 1.** Macro morphologies of (a) reduced iron powder (b) FeTi30 powder and (c) graphite powder

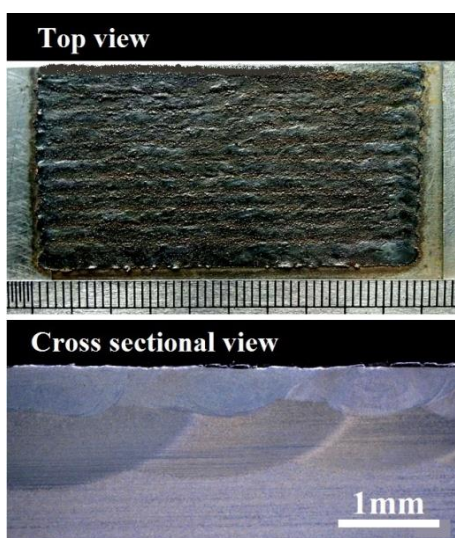
**Table 2.** Parameters of the laser cladding process

Laser power	Laser beam diameter	Scanning speed	Overlapping ratio	Argon gas flow rate
4000 W	4.0 mm	25 mm/s	30%	10 L/min

The phases of the layer were analyzed by X-ray diffraction with a Rigaku D/max-2500Pc diffractometer (Cu K $\alpha$ ) set to a working voltage and current of 50 kV and 30 mA, respectively. The step speed was 8 ( $^{\circ}$ )/min. The cladding layers were etched with a 4% nitric acid alcohol solution and the microstructure and morphology of the cladding layer were observed with a ZEISS SUPRA55 scanning electron microscope with a tube voltage of 15 kV and a Keyence (VHX-5000) optical microscope. Microhardness analysis was performed with a load of 200 g that was applied for 15 s. Polarization curves of the cladding layer and 42CrMo steel specimens were measured in 3.5 wt.% NaCl solution at 298 K and were conducted with a scan rate of 0.5 mV/s using a Gamry electrochemical workstation (Interface 1000). A saturated calomel electrode was used as the reference electrode and a platinum electrode was used as the counter electrode.

### 3. RESULTS AND DISCUSSION

Top view and cross-sectional view macrographs of the cladding layer are shown in Figure 2. The cladding layer was well-formed with a thickness of 0.4-0.8 mm, its surface was relatively flat, it had a good metallurgical bond with the substrate, and it did not have any defects such as cracks or pores.

**Figure 2.** Macrograph of the cladding layer: top view and cross-sectional view

The X-ray diffraction patterns of the cladding layer are shown in Figure 3, and the phases of the cladding layer were determined as  $\alpha$ -Fe,  $\gamma$ , and TiC. In combination with the microstructure of the cladding layer shown in Figure 4, the cladding layer phase was determined as lath martensite, retained austenite, and TiC.

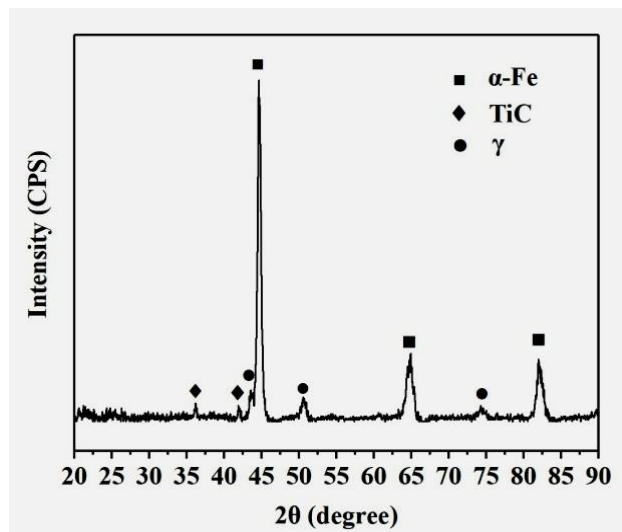


**Figure 3.** X-ray diffraction spectra of the cladding layer

Figure 4 (a) and (b) show the secondary electron images of the cladding layer and the distribution of the TiC particle size is shown in Figure 4 (c). The microstructure of the cladding layer was lath martensite, therefore, the cladding layer possessed high strength and toughness. The particle size of TiC ranged between 0.04  $\mu\text{m}$  and 1.10  $\mu\text{m}$ , and the average particle size was 0.25  $\mu\text{m}$ . Moreover, 98.9% of the TiC was on the submicron scale and 11.0 % was on the nano scale. The acquisition of the nano-submicron TiC could be attributed to the following two reasons: one was the gradient particle size of the initial alloy powders and the other was the high cladding and cooling speed. It has been previously shown that the refinement of carbides was mainly controlled by the graphite particle size, i.e., as the graphite particle size decreased from 180-270  $\mu\text{m}$  to 1.3  $\mu\text{m}$ , the average particle size of carbide decreased from 1.73 to 0.46  $\mu\text{m}$  [20, 22]. Emamian et al. indicated laser parameters have crucial role in establishing the TiC morphologies [23]. As a larger laser power and higher cladding speed were used, there was a higher cooling speed for the molten pool, which caused a higher supercooling degree for the TiC, and consequently, the nucleation rate of TiC increased [24].

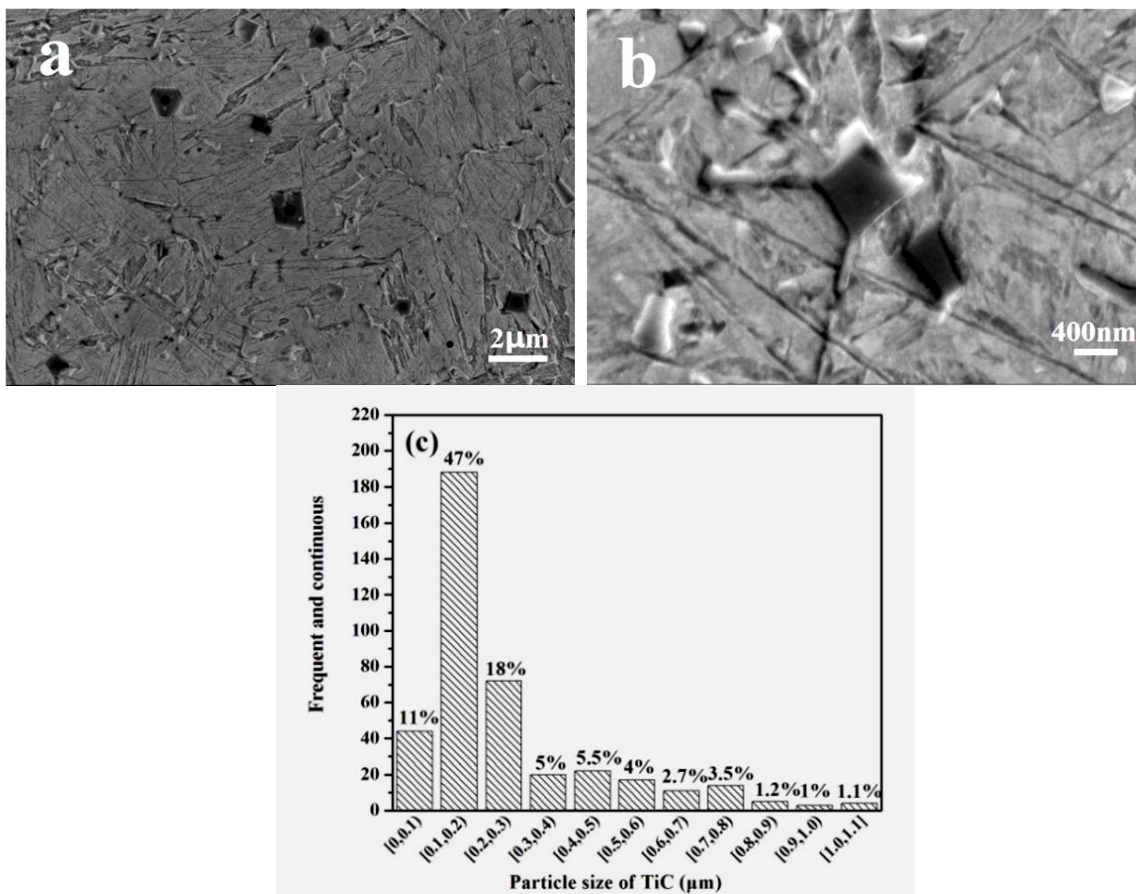


**Figure 4.** Secondary electron images of the cladding layer (a) magnified 5000 times (b) magnified 20000 times (c) the distribution of the TiC particle size

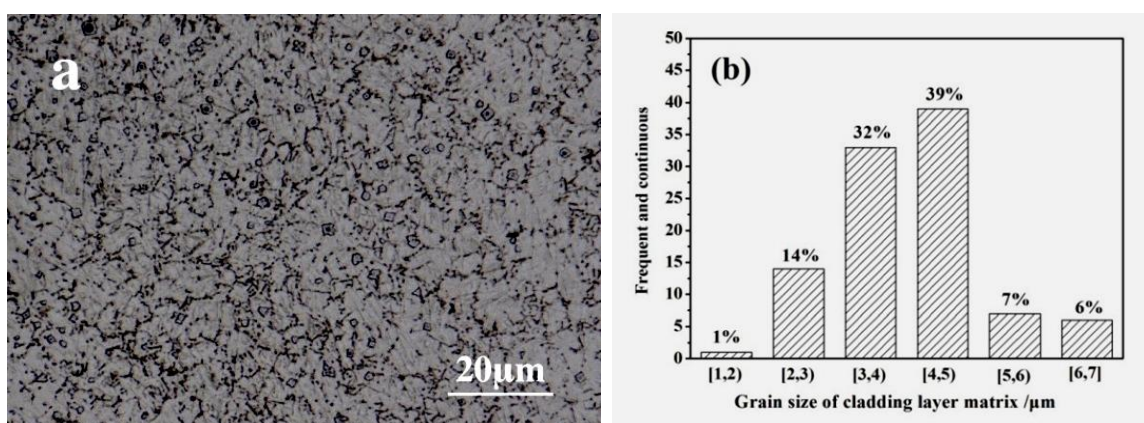
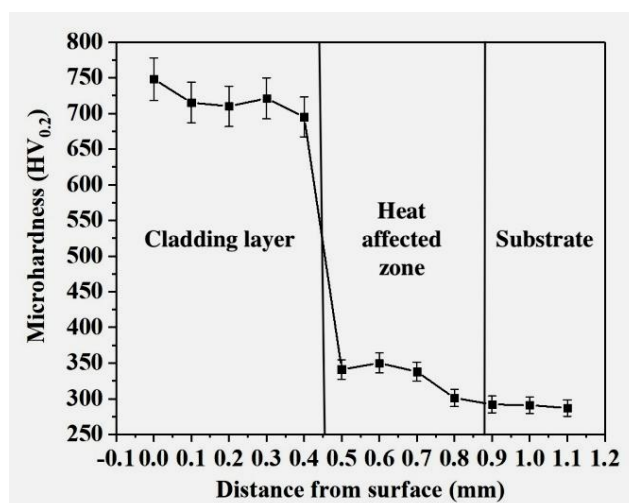


**Figure 5.** (a) Optical microscopy images and (b) the grain size distribution of the cladding layer matrix

Figure 5 shows the optical microscopy images of the Fe-based cladding layer matrix and its grain size distribution. The grain size of the cladding layer matrix ranged from 1.86 μm to 6.90 μm, with an average value of 4.08 μm. The TiC and austenite possessed the same crystal structure for the face centered cubic and, as the TiC nucleated and separated from the molten pool, it provided nucleation sites for the Fe-based layer matrix [25]. The lower the particle size of TiC, the greater the number of

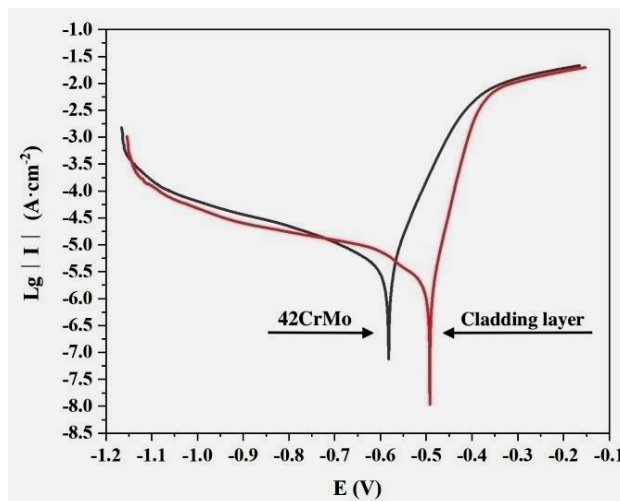
nucleation sites. As the TiC reached the nano-submicron scales, the number of crystallites of the cladding layer matrix increased significantly; thus, the grain size was refined.

Figure 6 shows the microhardness distribution curve on the cross-section of the cladding layer along the depth direction. The microhardness distribution curve was similar to a step-life function, which corresponded to the microhardness of the cladding layer, the heat affected zone, and the 42CrMo substrate. The average hardness of the cladding layer was approximately 720 HV<sub>0.2</sub>, which was much higher than that of the 42CrMo substrate. This high cladding layer hardness could be attributed to the dispersion strengthening effect of the nano-submicron scale TiC and the fine grain strengthening of the ultrafine-grained Fe-based cladding layer matrix.



**Figure 6.** Microhardness distribution on the cross-section of the cladding layer along the depth direction

Figure 7 shows the potentiodynamic polarization curves of the 42CrMo substrate and the cladding layer in 3.5 % NaCl solution. The curves were fitted using the Tafel method, and the fitting results are shown in Table 3. The corrosion potential of the cladding layer was higher than that of the 42CrMo steel; therefore, it had a smaller thermodynamic corrosion tendency. The current density of the cladding layer was  $45.18 \mu\text{Amp}\cdot\text{cm}^{-2}$ , which was more than two times lower than that of the 42CrMo steel. In the 42CrMo steel, corrosive cells formed between the ferrite and cementite, with Figure 8 (a) showing that the ferrite was corroded and contained many corrosion pits and trenches. As the TiC was refined into nano-submicron scales, although there were different corrosion potentials between the TiC and the cladding layer matrix, the galvanic corrosion effect was greatly reduced. Figure 8 (b) also shows that the surface of the cladding layer after corrosion was relatively flat compared with that of 42CrMo.



**Figure 7.** Potentiodynamic polarization curves of the 42CrMo substrate and the cladding layer in 3.5% NaCl solution

**Table 3.** Fitting results of the potentiodynamic polarization curves

Samples	E(V)	I (μAmp·cm <sup>-2</sup> )	Corrosion Rate(mm/a)
42CoMo	-0.582	10.80	0.126
Cladding layer	-0.494	45.18	0.053

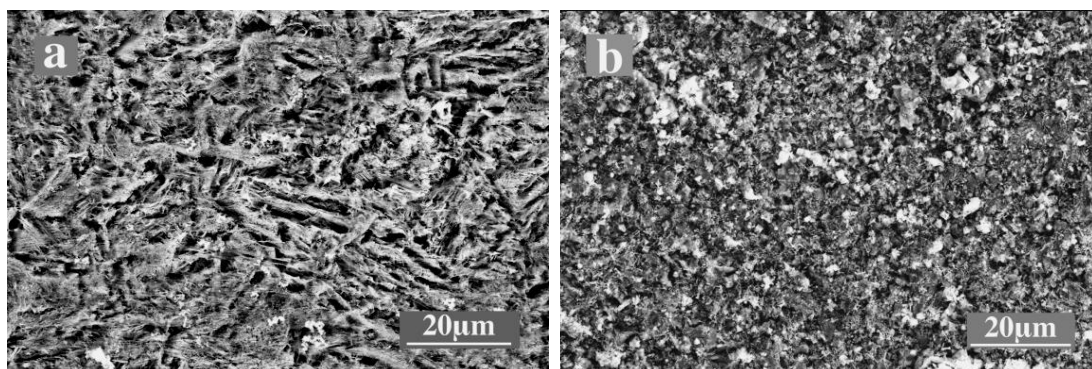


**Figure 8.** Corrosion morphologies of (a) 42CrMo substrate and (b) the cladding layer after running the polarization tests

#### 4. CONCLUSIONS

This present study showed that the nano-submicron TiC reinforced ultrafine-grained Fe-based laser cladding layers were prepared on the surface of 42CrMo steel and that the cladding layer was well formed and free from defects such as porosity and cracks. The microstructures of the layer were composed of lath martensite, retained austenite and TiC. The average particle size of TiC was 0.25 μm and ranged from 0.04 μm to 1.10 μm. Moreover, 98.9 % of the TiC reached the submicron scale, with

11.0 % reaching the nanoscale. The average grain size of the Fe-based matrix was 4.08  $\mu\text{m}$ , which reached the ultrafine-grained scale. Compared with the 42CrMo substrate, the hardness of the cladding layer increased by 425 HV0.2 and the corrosion resistance increased to 2.39 times.

#### ACKNOWLEDGEMENT

The work was supported by the National Natural Science Foundation of China (No.51605237), the Project funded by China Postdoctoral Science Foundation (2018M630775), the Key Research and Development Program of Shandong Province (2017GGX30136, 2018GGX103031), the Cooperation Fund of Qilu University of Technology (Shandong Academy of Sciences) for Young Doctors (2018BSHZ004).

#### References

1. J. Chen, Y. Zhou, C. Shi, D. Mao, *Metals*, 7 (2017) 435.
2. X.L. Lu, X.B. Liu, P.C. Yu, Y.J. Zhai, S.J. Qiao, M.D. Wang, Y.G. Wang, Y. Chen, *Appl. Surf. Sci.*, 355 (2015) 350.
3. K. Wang, B. Chang, Y. Lei, H. Fu, Y. Lin, *Metals*, 7 (2017) 551.
4. L. Yang, Z. Li, Y. Zhang, S. Wei, F. Liu, *Appl. Surf. Sci.*, 435 (2018) 1187.
5. R. Anandkumar, A. Almeida, R. Vilar, *Wear*, 282 (2012) 31.
6. C. Li, S. Sun, C. Liu, Q. Lu, P. Ma, Y. Wang, *J. Alloys Compd.*, 794 (2019) 236.
7. G. Muvvala, D. Patra Karmakar, A.K. Nath, *J. Alloys Compd.*, 740 (2018) 545.
8. C.K. Sahoo, M. Masanta, *Opt. Laser Eng.*, 67 (2015) 36.
9. L. Yanan, S. Ronglu, N. Wei, Z. Tiangang, L. Yiwen, *Opt. Laser Eng.*, 120 (2019) 84.
10. X. He, R.G. Song, D.J. Kong, *Opt. Laser Technol.*, 112 (2019) 339.
11. H. Liu, J. Liu, P. Chen, H. Yang, *Opt. Laser Technol.*, 118 (2019) 140.
12. D. Hong, Y. Niu, H. Li, X. Zhong, W. Tu, X. Zheng, J. Sun, *Sur. Coat. Technol.*, 374 (2019) 181.
13. C.K. Sahoo, L. Soni, M. Masanta, *Sur. Coat. Technol.*, 307 (2016) 17.
14. H. Ghazanfari, C. Blais, H. Alamdari, M. Gariépy, S. Savoie, R. Schulz, *Sur. Coat. Technol.*, 360 (2019) 29.
15. Z. Zhang, R. Kovacevic, *J. Manuf. Process.*, 38 (2019) 63.
16. X. Xu, G. Mi, L. Xiong, P. Jiang, X. Shao, C. Wang, *J. Alloys Compd.*, 740 (2018) 16.
17. H. Zhang, K. Chong, W. Zhao, Z. Sun, *Sur. Coat. Technol.*, 344 (2018) 163.
18. H. Zhang, Y. Zou, Z. Zou, D. Wu, *J. Alloys Compd.*, 622 (2015) 62.
19. H. Zhang, K. Chong, W. Zhao, Z. Sun, *Mater. Lett.*, 220 (2018) 44.
20. K. Chong, H. Zhang, G. Xiao, H. Xu, W. Zhao, *Int. J. Electrochem. Sci.*, 13 (2018) 6858.
21. A. Emamian, S.F. Corbin, A. Khajepour, *Sur. Coat. Technol.*, 206 (2011) 124.
22. H. Zhang, D. Wu, T. Luan, G. Xiao, W. Zhao, *Int. J. Electrochem. Sci.*, 14 (2019) 2208.
23. A. Emamian, S.F. Corbin, A. Khajepour, *Sur. Coat. Technol.*, 205 (2010) 2007.
24. B. Du, S.R. Paital, N.B. Dahotre, *Opt. Laser Technol.*, 45 (2013) 647.
25. M.J. Hamedi, M.J. Torkamany, J. Sabbaghzadeh, *Opt. Laser Eng.*, 49 (2011) 557.